PAPER

Gnetumgams A and B: two new 2-phenylbenzofuran derivatives from the lianas of *Gnetum montanum* with xanthine oxidase inhibitory activity

Truong Nhat Van Do, [acd] Minh Hien Nguyen, [bce] Hai Xuan Nguyen, [acd] Nhan Trung Nguyen [acd] and Mai Thanh Thi Nguyen [*acd]

Gnetum montanum ("Dây Gắm", Gnetaceae), traditionally employed in Vietnam for the treatment of rheumatism, chronic bronchitis, menstrual disorders, and as an antidote, was investigated for xanthine oxidase (XO) inhibitory constituents. Bioassay-guided fractionation led to the isolation of five 2-phenylbenzofurans, including two previously undescribed metabolites, gnetumgam A (**1**) and gnetumgam B (**2**), along with gnetifolin M (**3**), gnetifolin A (**4**), and gnetumelin B (**5**). Structures were unambiguously elucidated by comprehensive spectroscopic analyses (1D/2D NMR, HR-ESI-MS) and comparison with reference data. Among these, gnetumgam B (**2**) and gnetifolin M (**3**) exhibited notable XO inhibition (IC$_{50}$ = 111.7 and 113.1 μM, respectively), although less potent than the clinical agents allopurinol and febuxostat. Structure–activity relationship analysis revealed that substitution patterns on the benzyl ring and benzofuran nucleus strongly influenced activity, particularly *via* interactions within the molybdenum cofactor (MoCo) pocket. Molecular docking and dynamics simulations corroborated the experimental findings and underscored gnetumgam B (**2**) as a promising scaffold for further optimization toward next-generation XO inhibitors.

Introduction

Xanthine oxidase (XO), a member of the family of molybdenum-containing enzymes, comprises a molybdenum cofactor (MoCo) essential for redox reactions, two iron–sulfur clusters that mediate electron transfer, and a flavin adenine dinucleotide (FAD) serving as a prosthetic group.[1] XO catalyzes the conversion of hypoxanthine to uric acid through the purine degradation pathway.[2] Concomitantly, molecular oxygen is reduced, yielding reactive oxygen species (ROS) as byproducts, contributing to cellular oxidative stress.[3] Dysregulation of XO activity has been implicated in elevated blood uric acid levels and associated oxidative damage to normal tissues. Therefore, in gout management, pharmacological inhibition of XO is an important therapeutic strategy, as XO inhibitors block the final steps of uric acid production, mitigating urate accumulation and potentially attenuating systemic comorbidities linked to elevated uric acid levels.[4]

Allopurinol and febuxostat, the two main XO inhibitors, are commonly used in gout treatment and hyperuricemia.[5] Allopurinol is a purine analog that competes with hypoxanthine and xanthine as substrates for XO. Additionally, allopurinol itself is metabolized by XO to produce oxypurinol that can bind tightly with the reduced form of XO, thereby contributing to its inhibition of XO.[6] Allopurinol is also metabolized by other enzymes to produce nucleotide analogues which are able to inhibit purine nucleoside phosphorylase (PNP), a key enzyme in purine metabolism, and orotidine-5′-monophosphate decarboxylase (OMPDC), which is involved in RNA and DNA synthesis.[7] The off-target effects may account for some side effects of allopurinol. Whereas, febuxostat is a non-purine XO inhibitor that does not interfere with other pathways. Compared with allopurinol, febuxostat can inhibit both reduced and oxidized forms of XO.[8] However, febuxostat is primarily metabolized in liver and has been associated with potential cardiovascular risks.[9] Therefore, it is necessary to seek for the new potential compounds with non-purine structures that can selectively inhibit XO with minimizing the side effects.

[a]Faculty of Chemistry, University of Science, Ho Chi Minh City, 227 Nguyen Van Cu Street, Cho Quan Ward, Ho Chi Minh City 70000, Vietnam
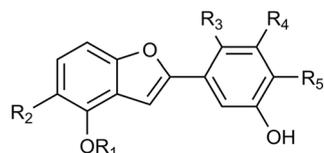
[b]University of Health Sciences, Vietnam National University Ho Chi Minh City, YA1 Administrative Building, Hai Thuong Lan Ong Street, VNUHCM Urban Area, Linh Xuan Ward, Ho Chi Minh City 70000, Vietnam

[c]Vietnam National University Ho Chi Minh City, Linh Xuan Ward, Ho Chi Minh City 70000, Vietnam. E-mail: nttmai@hcmus.edu.vn; Tel: +84-907-426-331

[d]Research Lab for Drug Discovery and Development, University of Science, Ho Chi Minh City, Vietnam

[e]Research Center for Discovery and Development of Healthcare Products, Vietnam National University Ho Chi Minh City, Ho Chi Minh City, Vietnam

Fig. 1   Chemical structures of compounds 1–5.

Gnetum montanum, commonly known in Vietnam as Dây Gắm, belongs to the Gnetaceae family and was first reported by Markgraf in 1930.[10] According to traditional medicine, various parts of *G. montanum* are utilized to treat rheumatism, chronic, bronchitis, menstrual disorders, and as an antidote.[11–13] Previous studies on the chemical composition of *G. montanum* have identified numerous valuable compounds, including flavonoids, stilbenes, lignans, and alkaloids.[14–19] Both domestic and international studies have shown that extracts and isolated compounds from this species display diverse biological activities, including antibacterial, antiviral, antioxidant, antihyperuricemic, anti-inflammatory, anticancer, and hypoglycemic effects.[11,19–22] In a continued study on the biological activity screening of various medicinal plants in Vietnam, we have discovered that the lianas methanol extract of *G. montanum* had the greatest potential for biological activities, as evidenced by its inhibitory activity against XO with $IC_{50} = 76.7$ μg mL^{-1}. By column chromatography and preparative TLC methods combined with modern spectroscopic methods, five 2-phenylbenzofurans were isolated, consisting of two previously undescribed compounds, gnetumgam A (**1**) and gnetumgam B (**2**) together with three known compounds. The known compounds were identified by analysis of their spectroscopic data and comparison with literature data as gnetifolin M (**3**),[23] gnetifolin A (**4**),[21] and gnetumelin B (**5**) (Fig. 1).[21] This present study details the isolation procedure and structural elucidation of two new compounds, along with an assessment of their XO inhibitory activity through both *in vitro* and *in silico* experiments.

Results and discussion

Compound **1** obtained a brown amorphous solid and the molecular formula of **1** and showed a sodium adduct molecular ion peak $[M + H_2O + Na]^+$ at *m/z* 357.0948 in the HR-ESI-MS (calc. for $C_{17}H_{18}O_7Na^+$, 357.0950), consistent with the molecular formula $C_{17}H_{16}O_6$. The IR spectrum illustrated the absorption of hydroxyl (3408 cm^{-1}) and phenyl (1600 and 1488 cm^{-1}) groups. The ^{1}H-NMR spectrum of **1** showed signals of two *ortho*-coupling aromatic protons [δ_H 6.90 (1H, d, *J* = 8.7 Hz; H-6) and 7.10 (1H, d, *J* = 8.7 Hz; H-7)], two *meta*-coupling aromatic protons [δ_H 6.98 (1H, d, *J* = 1.9 Hz; H-2′) and 7.08 (1H, d, *J* = 1.9 Hz; H-6′)], an isolated olefinic proton [δ_H 7.00 (1H, s;

Table 1   The ^{1}H (500 MHz) and ^{13}C (125 MHz) NMR spectroscopic data of compounds **1** and **2**

No.	**1**[a] δ_H (*J* in Hz)	δ_C	**2**[b] δ_H (*J* in Hz)	δ_C
2		155.8		155.0
3	7.00 s	98.6	7.23 s	99.3
3a		120.4		119.6
4		138.3		157.3
5		142.8	6.68 d (7.8)	108.9
6	6.91 d (8.7)	112.3	7.11 dd (8.3, 7.8)	126.0
7	7.10 d (8.7)	105.9	7.04 d (8.3)	103.5
7a		150.6		152.0
1′		126.4		127.1
2′	6.98 s (1.9)	101.4		154.5
3′		152.8	7.08 s	101.5
4′		136.4		138.0
5′		149.8		151.8
6′	7.08 d (1.9)	105.2	7.08 s	106.3
4-OCH$_3$	4.13 s	60.4		
2′-OCH$_3$			3.95 s	56.4
3′-OCH$_3$	3.97 s	56.2		
4′-OCH$_3$	3.95 s	61.3	3.82 s	60.9
4-OH			8.89 s	
5′-OH			8.09 s	

^{a} In CDCl$_3$. ^{b} In CD$_3$COCD$_3$.

H-3)], and signals of three methoxyl groups [δ_H 4.13 (3H, s, 4-OCH$_3$), 3.97 (3H, s, 3′-OCH$_3$), and 3.95 (3H, s; 4′-OCH$_3$)] (Table 1). The ^{13}C-NMR and DEPT spectra of compound **1** displayed resonances for 17 carbons, including twelve aromatic carbons [δ_C 101.4–152.8], two olefinic carbons [δ_C 155.8 (C-2) and 98.6 (C-3)], and three methoxyl carbons [δ_C 60.4 (4-OCH$_3$), 61.3 (4′-OCH$_3$), and 56.2 (3′-OCH$_3$)] (Table 1). These data indicated that compound **1** was the 2-phenylbenzofuran skeleton consisting of three methoxyl and two hydroxyl groups. In the phenyl ring (C-1′–C-6′), two *meta*-coupling aromatic protons were determined as H-2′ and H-6′ because of their HMBC correlations with the oxygenated olefinic carbon δ_C 155.8 (C-2) of the benzofuran unit. Moreover, the aromatic proton H-2′ and the only olefinic proton H-3 had cross-peaks with an aromatic carbon δ_C 126.4, so it was consistent with C-1′. The protons (H-2′ and H-6′) and the methoxyl protons δ_H 3.95 correlated with an oxygenated aromatic carbon δ_C 136.4; therefore, the methoxyl group was attached to C-4′. The position C-3′ carried the other methoxyl group based on the HMBC correlation of the methoxyl protons δ_H 3.97 with an oxygenated aromatic carbon δ_C 152.8, meanwhile C-5′ (δ_C 149.8) carried a free hydroxyl group due to the low-field shifted ^{13}C chemical shifts of it. Regards to the benzofuran unit, the double bond corresponded to C-2 and C-3 bearing hydrogen based on an HSQC correlation (Fig. 2). The HMBC correlations of H-3 and the remaining methoxyl protons δ_H 4.13 with an oxygenated aromatic carbon δ_C 138.3 suggested this methoxyl group bonded to C-4. Furthermore, C-7a was established by the HMBC correlations of H-3 and an *ortho*-coupling aromatic proton δ_H 6.90 with an oxygenated aromatic carbon δ_C 150.6. The other

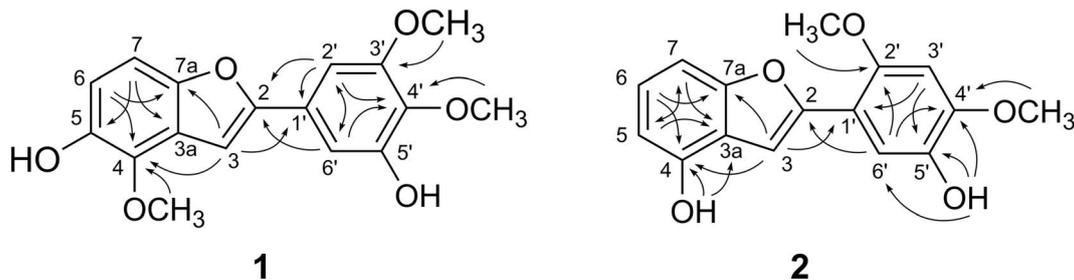© 2026 The Author(s). Published by the Royal Society of Chemistry

Fig. 2   HMBC correlations of compounds 1 and 2.

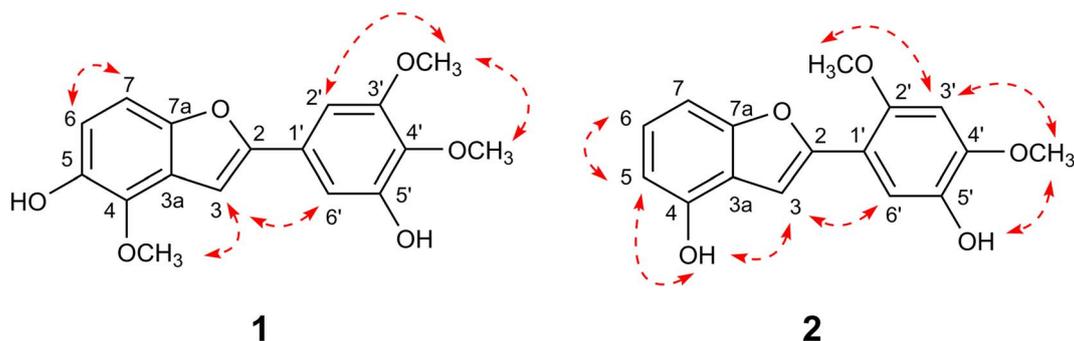
Fig. 3   NOESY correlations of compounds 1 and 2.

ortho-coupling aromatic proton δ_H 7.10 presented the interactions with the remaining aromatic carbon δ_C 142.8 and a substituted aromatic carbon δ_C 120.4; consequently, they were identified to be as C-5, bearing a free hydroxyl group and C-3a, respectively. This also affirmed two *ortho*-coupling aromatic protons to be H-6 and H-7. Finally, in the NOESY spectrum of compound 1, it was obvious that the NOESY correlations of the methoxyl proton 3′-OCH$_3$ (δ_H 3.97) with the aromatic proton H-2′ (δ_H 6.98) and another methoxyl proton 4′-OCH$_3$ (δ_H 3.95) suggested two adjacent methoxyl groups (Fig. 3). In addition, NOESY correlations were detected between the olefinic proton H-3 (δ_H 7.00) and the aromatic proton H-6′ (δ_H 7.08), as well as the methoxyl protons 4-OCH$_3$ (δ_H 4.13). Thus, the structure of gnetumgam A (1) was elucidated as shown.

Compound 2 was obtained as a brown amorphous solid. The HR-ESI-MS spectrum of compound 2 gave a *quasi*-molecular ion peak at *m/z* 285.0767 [M–H]$^-$ (calcd. for 285.0768, C$_{16}$H$_{13}$O$_5$), corresponding to the molecular formula C$_{16}$H$_{14}$O$_5$. The IR absorption bands of 2 demonstrated the presence of hydroxyl (3408 cm^{-1}) and phenyl (1600, 1488 cm^{-1}) groups. The ^{1}H-NMR spectrum of 2 exhibited signals of two *para*-coupling aromatic protons [δ_H 7.08 (1H, s, H-3′) and 7.08 (1H, s, H-6′)], a 1,2,3-trisubstituted aromatic moiety [δ_H 6.68 (1H, d, *J* = 7.8 Hz, H-5), 7.11 (1H, dd, *J* = 8.3 and 7.5 Hz, H-6), and 7.04 (1H, d, *J* = 8.3 Hz, H-7)], an isolated olefinic proton [δ_H 7.23 (1H, s, H-3)], and signals of two methoxyl groups [δ_H 3.95 (3H, s, 2′-OCH$_3$) and 3.82 (3H, s, 4′-OCH$_3$)] (Table 1). The ^{13}C-NMR spectrum of 2 showed the resonance signals of 16 carbons, of which twelve aromatic carbons [δ_C 101.5–157.3], two olefinic carbons [δ_C 155.0 (C-2) and 99.3 (C-3)], and two methoxyl carbons [δ_C 56.4

(2′-OCH$_3$) and 60.9 (4′-OCH$_3$)] (Table 1). These data of compound 2 also indicated the 2-phenylbenzofuran skeleton, consisting of two methoxyl and two hydroxyl groups. The HMBC correlations of two methoxyl protons (δ_H 3.95 and 3.82) with the oxygenated aromatic carbons (δ_C 154.5 and 138.0) suggested the location of two methoxyl groups at C-2′ and C-4′ (Fig. 2). The two free hydroxyl groups were determined to be as aromatic carbons at C-4 and C-5′ (δ_C 157.3 and 151.8) due to the HMBC correlations and low-field shifted ^{13}C chemical shifts of them. The NOESY spectrum of compound 2 revealed a correlation between the olefinic proton H-3 (δ_H 7.23) and the aromatic proton H-6′ (δ_H 7.08), as well as hydroxyl proton 4-OH (δ_H 8.89). Additional NOESY correlations were observed between aromatic protons H-5 (δ_H 6.68) and H-6 (δ_H 7.11), and also hydroxyl proton 4-OH (δ_H 8.89). Moreover, NOESY cross-peaks were detected between the aromatic proton H-3′ (δ_H 7.08) and the methoxyl protons 2′-OCH$_3$ (δ_H 3.95), as well as the methoxyl protons 4′-OCH$_3$ (δ_H 3.82). Thus, the structure of gnetumgam B (2) was concluded as shown (Fig. 3).

The *in vitro* xanthine oxidase (XO) inhibitory activities of the isolated compounds were evaluated across various concentrations (250-1 μM) (Table 2). The results showed that among the tested compounds, gnetumgam B (2) and gnetifolin M (3) exhibited the most promising XO inhibitory activity, with IC$_{50}$ values of 111.7 μM and 113.1 μM, respectively, compared to the positive control, allopurinol (IC$_{50}$ = 2.5 μM) and febuxostat (IC$_{50}$ = 0.020 μM).

XO is a homodimeric molybdenum-dependent enzyme comprising three functional domains: a molybdenum cofactor (MOCO) domain, two iron–sulfur (Fe$_2$S$_2$) clusters, and a flavin

Table 2 Xanthine oxidase inhibitory activity of isolated compounds

Compounds	Inhibitory percentage (I. %)				IC$_{50}$ (μM)
	250 μM	100 μM	50 μM	25 μM	
Gnetumgam A (**1**)	34.5 ± 2.0	19.1 ± 1.5	—	—	>250
Gnetumgam B (**2**)	92.8 ± 3.5	46.9 ± 2.8	34.2 ± 1.7	18.2 ± 2.9	**111.7 ± 1.8**
Gnetifolin M (**3**)	71.6 ± 1.2	47.9 ± 2.3	39.4 ± 2.6	—	**113.1 ± 2.2**
Gnetifolin A (**4**)	52.8 ± 1.6	41.5 ± 2.5	23.3 ± 1.0	13.2 ± 1.1	**196.6 ± 3.4**
Gnetumelin B (**5**)	19.2 ± 2.4	4.5 ± 1.0	—	—	>250

Compounds	Inhibitory percentage (I. %)				IC$_{50}$ (μM)
	10 μM	5 μM	2.5 μM	1 μM	
Alopurinol	52.8 ± 1.6	41.5 ± 2.5	23.3 ± 1.0	13.2 ± 1.1	**2.54 ± 0.10**

Compounds	Inhibitory percentage (I. %)				IC$_{50}$ (μM)
	0.1 μM	0.05 μM	0.025 μM	0.01 μM	
Febuxostat	93.2 ± 2.1	87.5 ± 1.3	55.5 ± 1.3	37.0 ± 4.4	**0.020 ± 0.003**

Table 3 Binding energy and interactions between key amino acids of the xanthine oxidase and compounds **1–5**, alopurinol, and febuxostat

Compounds	Docking score (kcal mol^{-1})	Key residues
Gnetumgam A (**1**)	−7.5	Alkyl: Leu648, Leu873, Pro1076 π-alkyl: Val1011, Leu1014, Ala1078, Ala1079 H-bond: Glu802, Ser876, Arg880, Phe1009, Thr1010 π–π stacked/π–π T shaped: Phe914, Phe1009
Gnetumgam B (**2**)	−8.6	Alkyl: Ala910, Ala1078 π-alkyl: Leu648, Leu873, Phe914, Val1011 H-bond: Thr1010, Arg880, Glu1261 π–π stacked/π–π T shaped: Phe914, Phe1009 π–σ: Leu1014 Unfavorable donor–donor: Ser876
Gnetifolin M (**3**)	−9.3	Alkyl: Ala910, Ala1078 π-alkyl: Leu648, Leu873, Val1011, Leu1014, Ala1078, Ala1079 H-bond: Glu802, Ser876, Ser1008, Thr1010, Ala1079 π–π stacked/π–π T shaped: Phe914, Phe1009 π–σ: Phe914 Unfavorable donor–donor: Arg880
Gnetifolin A (**4**)	−9.0	Alkyl: Leu648, Leu873, Pro1076 Pi-alkyl: Leu648, Leu873, Val1011, Leu1014, Ala1078 H-bond: Glu802, Arg880, Ser1008, Glu1261 π–π stacked/π–π T shaped: Phe914, Phe1009
Gnetumelin B (**5**)	−7.7	Alkyl: Leu648, Leu873, Pro1076 π-alkyl: Val1011, Phe1013, Leu1014, Ala1078, Ala1079 H-bond: Arg880, Thr1009, Thr1010 π–π stacked/π–π T shaped: Phe914, Phe1009 Unfavorable donor–donor: Arg880
Allopurinol	−6.9	π-alkyl: Ala1078, Ala 1079 π–π stacked/π–π T shaped: Phe914, Phe1009 H-bond: Glu802, Ala1079 Unfavorable donor–donor: Arg880
Febuxostat	−8.9	Alkyl: Leu648, Leu1014, Ala1078, Ala1079 π-alkyl: Leu873, Val1011, Phe1013 H-bond: Asn768, Arg880, Thr1010 π–π stacked/π–π T shaped: Phe914, Phe1009 π–σ: Phe914
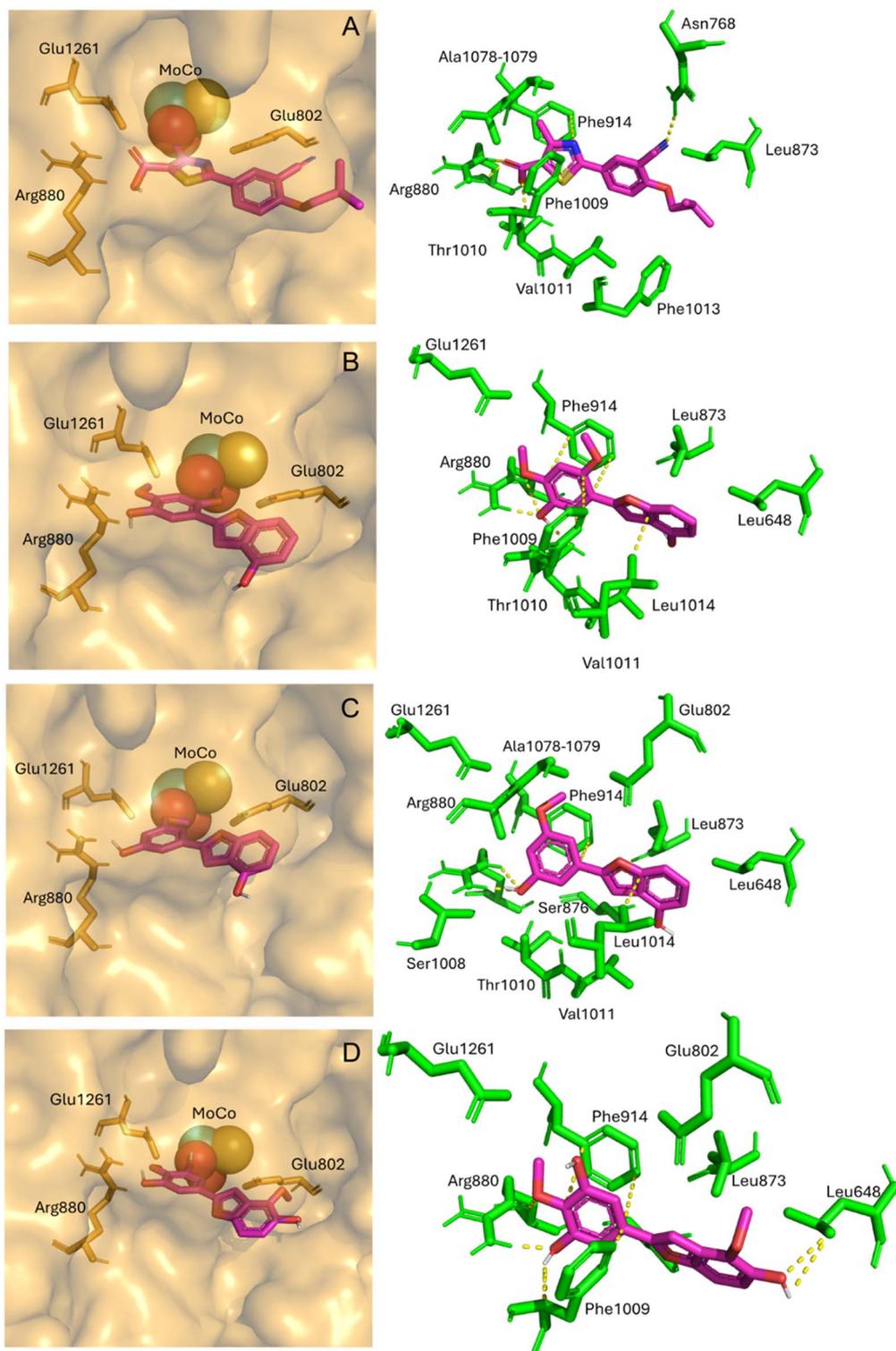
Fig. 4 Binding poses and key interactions of febuxostat (A), gnetumgam B (B), gnetifolin M (C), and gnetifolin A (D) with residues at the MOCO active site.

adenine dinucleotide (FAD) domain. Catalysis is centered at MOCO, where clinically validated inhibitors such as allopurinol and febuxostat engage the pocket, stabilizing interactions with Phe914, Phe1009, Arg880, and Thr1010 while recapitulating key features of substrate binding.

Docking analysis revealed that gnetumgam B, gnetifolin M, and gnetifolin A exhibit binding affinities comparable to febuxostat (Table 3 and Fig. 4). These ligands consistently engage in π–π interactions with Phe914 and Phe1009 through their benzyl scaffolds, while simultaneously forming hydrogen
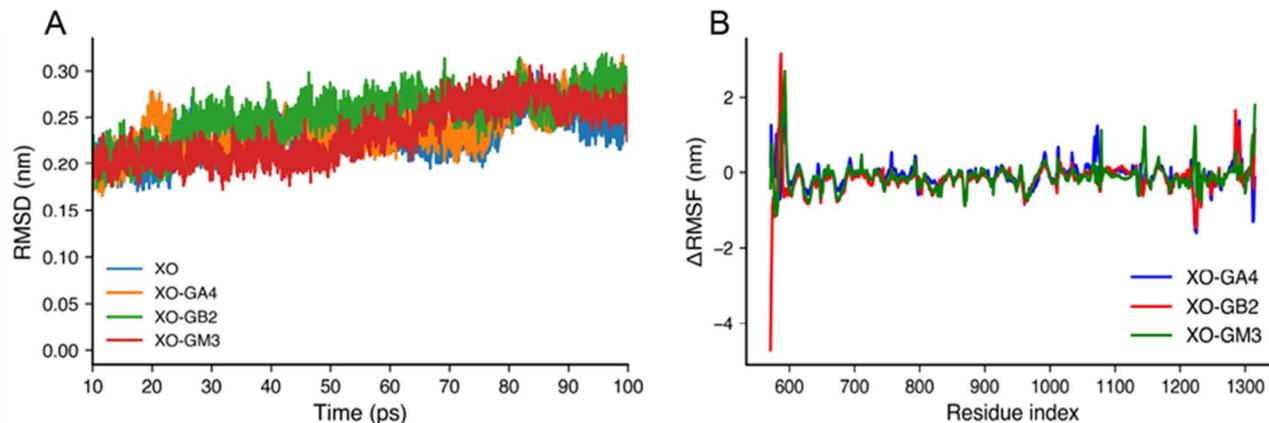
Fig. 5 Molecular dynamics simulations of the xanthine oxidase (XO) complexes. (A) RMSD trajectories of XO in complex with gnetumgam B (XO-GB2), gnetifolin M (XO-GM3), and gnetifolin A (XO-GA4), compared with the apo enzyme (XO) over the course of the simulation. (B) ΔRMSF profiles of the same systems, illustrating residue-specific stabilization (negative ΔRMSF) or destabilization (positive ΔRMSF) upon ligand binding relative to the apo enzyme.

bonds with Arg880 and Thr1010, closely mimicking the binding mode of febuxostat with XO (Fig. 4A). Importantly, gnetifolin M (**3**) and gnetifolin A (**4**) establish an additional hydrogen bond with Glu802 *via* their benzofuran moiety, a feature that contributes to their improved docking scores (Fig. 4C and D). These interactions parallel the role of the benzofuran ring in reinforcing activity at the MOCO site. Despite these favorable interactions, the presence of unfavorable donor–donor contacts may attenuate the *in vitro* activities of gnetumgam B and gnetifolin M relative to febuxostat and allopurinol (Fig. 4B and C, Table 3).

The three top-ranked docking complexes were subjected to molecular dynamics simulations (MD) to further assess their structural stability and dynamic behavior. Root-mean-square deviation (RMSD) was evaluated to investigate the overall stability of the complexes during the trajectories, while root-mean-square fluctuation (RMSF) was used to access residue-level flexibility and changes at the binding interface (Fig. 5). The RMSD trajectories indicated that all complexes attained equilibrium after 10 ps and remained stable throughout the simulation, with values consistently below 0.3 nm, indicating the robustness of ligand binding to XO. RMSF analysis provided residue-level insights, wherein positive ΔRMSF values denote local destabilization and negative values reflect stabilization upon complex formation. Notably, the majority of residues displayed negative ΔRMSF, suggesting overall stabilization of the protein upon complex formation (Fig. 5B). These findings are in line with prior reports on oxipurinol, which is stabilized within the active site by residues Glu802, Arg880, Phe914, Phe1005, Phe1009, and Ala910. Conversely, residues proximal to the MOCO domain were predominantly destabilizing.[24] The consistency of our RMSF profiles with previously published data further validates the reliability of our simulations.

The combined *in vitro* and *in silico* analyses highlight the potential of benzofuran-derived natural products as a new class of XO inhibitors. These compounds capitalize on their non-purine scaffolds while partially mimicking the binding

features of febuxostat. Nevertheless, the moderate inhibitory activities observed underscore the need for further structural optimization, particularly through judicious modification of substituents on the benzyl ring and benzofuran moiety, to mitigate unfavorable interactions. In addition to direct active-site binding, the stabilizing or destabilizing effects exerted at the MOCO region appear to modulate the inhibitory potency of these ligands. Among the five benzofuran derivatives tested, new gnetumgam B (**2**) demonstrated relatively good XO inhibition *in vitro*, a result that was consistent with molecular docking and molecular dynamics simulations.

Experimental

General

IR spectra were performed on a JASCO FT/IR-6600 spectrometer (JASCO International Co., Ltd). HR-ESI-MS were taken with a Q-TOF spectrometer (Shimadzu Co., Ltd, Japan). NMR spectra were measured on a Bruker Avance III 500 spectrometer (Bruker BioSpin AG) in $CDCl_3$ and CD_3COCD_3 as an internal standard. The absorbance (OD) was conducted on a Shimadzu UV-1800 spectrophotometer (Shimadzu Pte., Ltd, Singapore). Silica gel 60 (40–63 μm) were bought from Scharlau (Scharlab, S. L., Spain). Analytical and preparative TLCs were carried out on precoated Kieselgel 60 F_{254} (Merck KGaA, Germany). Other chemicals were of the highest grade available.

Plant material

The lianas of *Gnetum montanum* was collected in Hoa Binh Province, Vietnam, in August 2019 and identified by Dr Ha Thanh Bui, Department of Traditional Medicine, Military Hospital 103 (Vietnam Military Medical Academy). The voucher sample of the lianas part (MCE0065) was deposited at the Division of Medicinal Chemistry, Faculty of Chemistry, University of Science, VNU-HCMC.

Extraction and isolation

The dried powder lianas of *Gnetum montanum* (6.5 kg) were exhaustively extracted in a Soxhlet extractor with *n*-hexane, EtOAc, and MeOH in turn to yield *n*-hexane – (24.5 g), EtOAc – (150.0 g), and MeOH – (585.0 g) soluble extracts, respectively. The EtOAc-soluble extract was separated by a silica gel column (10 × 120 cm) and eluted with MeOH–CHCl$_3$ mixtures (v/v, 0 : 100 → 100 : 0) to obtain 15 fractions (Fr.1–15). Fraction Fr.4 (0.6 g) was applied to a silica gel column chromatography with an EtOAc-*n*-hexane gradient system (0–50%) to yield seven subfractions (Fr.4.1–Fr.4.7). Subfraction Fr.4.6 was subjected to a silica gel column chromatography and eluted with chloroform-*n*-hexane to yield compound **1** (3.0 mg). Fraction Fr.5 (5.7 g) was applied to a silica gel column chromatography and eluted with EtOAc-*n*-hexane gradient mixtures (v/v, 0 : 100 → 100 : 0) to yield 18 subfractions (Fr.5.1–Fr.5.18). Subfraction Fr.5.15 (191.0 mg) was subjected to a silica gel column chromatography and eluted with EtOAc-*n*-hexane (v/v, 0 : 100 → 50 : 0) to yield compound **5** (13.6 mg).Fraction Fr.6 (1.1 g) were chromatographed with an acetone-*n*-hexane gradient system (v/v, 0 : 100 → 30 : 70), to give six subfractions (Fr.6.1–Fr.6.6). Subfraction Fr.6.3 (455.1 mg) was subjected to silica gel column chromatography an acetone-*n*-hexane gradient system (0–50%) and then separated by preparative TLC using acetone-*n*-hexane (20 : 80) to give compound **2** (8.0 mg). Fraction Fr.8 (2.1 g) was passed over a silica gel column with an acetone-*n*-hexane gradient system (v/v, 0 : 100 → 100 : 0) to yield seven subfractions (Fr.8.1–Fr.8.7). Subfractions Fr.8.2 (90.8 mg) was subjected to silica gel column chromatography with MeOH-CHCl$_3$ mixtures (v/v, 0 : 100 → 30 : 70) to afford compound **4** (42.0 mg). Subfraction Fr.8.3 (147.6 mg) was further separated by silica gel column chromatography with EtOAc-*n*-hexane mixtures (0 : 100 → 100 : 0) and purified by preparative TLC using isopropyl alcohol-*n*-hexane (10 : 90) to give compound **3** (8.0 mg).

Compound 1: brown, amorphous solid; IR ν_{max} (KBr plate) 3408, 1600, 1488 cm^{-1}; ^{1}H and ^{13}C NMR (acetone-d_6, 500 MHz, see Table 1); HRESIMS *m/z* 357.0948 [M + H$_2$O + Na]$^+$ (calc. for C$_{17}$H$_{18}$O$_7$Na$^+$, 357.0950).

Compound 2: brown, amorphous solid; IR ν_{max} (KBr plate) 3408, 1600, 1488 cm^{-1}; ^{1}H and ^{13}C NMR (acetone-d_6, 500 MHz, see Table 1); HRESIMS *m/z* 285.0767 [M–H]$^-$ (calcd. for C$_{16}$H$_{13}$O$_5$).

Xanthine oxidase inhibitory activity assay

The isolated compounds were dissolved in DMSO and utilized in the experiment at concentrations ranging from 25 to 250 μM. Subsequently, 50 μL of enzyme solution (XO 0.05 U mL^{-1}) was added to the mixture and incubated at room temperature for 15 minutes. Following this, 450 μL of 150 μM xanthine was introduced into the mixture and the reaction was further incubated at room temperature for 30 minutes. The reaction was then terminated by adding 100 μL of 1 N HCl and the inhibitory activity was determined by measuring the absorbance at 293 nm using a Shimadzu UV-1800 spectrophotometer. The xanthine oxidase inhibitory activity was expressed as the percentage of inhibition, calculated using the formula: [(1 − Abs$_{sample}$/Abs$_{control}$) × 100%]. The results were presented as mean ± standard error ($n = 3$). Allopurinol, a well-known xanthine oxidase inhibitor, was used as a reference under the same experimental conditions to assess the xanthine oxidase inhibitory activity of the test samples.

Molecular docking and molecular dynamics simulation

Molecular docking was carried out for the complexes formed between xanthine dehydrogenase/oxidase (PDB ID: 1FIQ) and compounds **1–5**, as well as the reference drugs allopurinol and febuxostat. The workflow included the following steps: ligand structures in SMILES format were converted into 3D structures using OpenBabel. Prior to docking, both protein and ligand structures were processed using the Dock Prep tool in UCSF Chimera (version 1.17.3), which involved removing nonstandard residues, adding missing hydrogen atoms, and assigning appropriate charges. Docking simulations were conducted using AutoDock Vina (version 1.1.2). The docking was targeted at the active site of xanthine oxidase, with a grid box size of 25.69 Å × 26.87 Å × 23.30 Å, centered at coordinates $x = 21.34$, $y = 14.24$, and $z = 115.62$. Visualization of 3D binding conformations was performed using PyMOL 3.0, while Biovia Discovery Studio 21.1 was utilized to generate 2D interaction diagrams between the enzyme and the ligands.

Molecular dynamics (MD) simulations were performed on both the native xanthine oxidase and its docked complexes with the ligands using GROMACS version 2024.1. The protein topology was generated using the CHARMM36 force field, along with the TIP3P water model as recommended by GROMACS. Ligand topologies were obtained from the CGENFF web server and converted into GROMACS-compatible formats *via* a Python script provided by the Mackerell lab. Topology files for the protein and ligands were manually combined using a text editor. The complete system was then placed in a dodecahedral simulation box, ensuring at least 1 nm spacing between the solute and box boundary. Solvation was carried out using the SPC216 explicit water model, and the system was neutralized with 20 Na$^+$ ions. Energy minimization was conducted using the steepest descent algorithm until the maximum force was reduced below 100 kJ mol^{-1} nm^{-1}. Equilibration followed in two stages under position restraints, each using a 2 fs time step over 1 ns. The first stage used an NVT ensemble with a V-rescale thermostat set at 300 K, while the second employed an NPT ensemble with a C-rescale barostat maintained at 1 bar. Long-range electrostatic interactions were treated using the Particle Mesh Ewald (PME) method, and a 1 nm cutoff was applied for both short-range electrostatics and van der Waals forces. Hydrogen bond constraints were applied using the LINCS algorithm during both equilibration and production phases. The final production run was executed for 100 ns, with trajectory data recorded every 10 ps.

Author contributions

The manuscript was written through the contributions of all authors. All authors have given approval to the final version of the manuscript.

Conflicts of interest

No potential conflict of interest was reported by the authors.

Abbreviations

COSY	Correlation spectroscopy
d	Doublet
dt	Doublet of triplet
DEPT	Distortionless enhancement by polarization transfer
HMBC	Heteronuclear multiple bond correlation
HSQC	Heteronuclear single quantum correlation
HR-ESI-MS	High-resolution electrospray ionization mass spectrometry
IC_{50}	Half-maximum inhibitory concentration
IR	Infrared
J	Coupling constant
m	Multiplet
NMR	Nuclear magnetic resonance
NOESY	Nuclear overhauser effect spectroscopy
s	Singlet
t	Triplet
TLC	Preparative thin-layer chromatography
XO	Xanthine oxidase

Data availability

Spectra for all compounds are presented in the supporting information (SI). See DOI: https://doi.org/10.1039/d5ra08293e.

Acknowledgements

References

1 T. Nishino and K. Okamoto, The role of the [2Fe–2S] cluster centers in xanthine oxidoreductase, *J. Inorg. Biochem.*, 2000, **82**(1), 43–49.

2 C. Han, Y. Wu, J. Rong, Q. Xia and D. Du, Unveiling the emerging role of xanthine oxidase in acute pancreatitis: beyond reactive oxygen species, *Antioxidants*, 2025, **14**(1), 95.

3 K. Jomova, R. Raptova, S. Y. Alomar, S. H. Alwasel, E. Nepovimova, K. Kuca and M. Valko, Reactive oxygen species, toxicity, oxidative stress, and antioxidants: chronic diseases and aging, *Arch. Toxicol.*, 2023, **97**(10), 2499–2574.

4 C. Chen, J. M. Lü and Q. Yao, Hyperuricemia-related diseases and xanthine oxidoreductase (XOR) inhibitors: an overview, *Med. Sci. Monit.: Int. Med. J. Exp. Clin. Res.*, 2016, **22**, 2501–2512.

5 A. F. G. Cicero, F. Fogacci, R. I. Cincione, G. Tocci and C. Borghi, Clinical effects of xanthine oxidase inhibitors in hyperuricemic patients, *Med. Princ. Pract.: Int. J. Kuwait Univ. Health Sci. Centre*, 2021, **30**(2), 122–130.

6 Y. Tayama, K. Sugihara, S. Sanoh, K. Miyake, S. Kitamura and S. Ohta, Xanthine oxidase and aldehyde oxidase contribute to allopurinol metabolism in rats, *J. Pharm. Health Care Sci.*, 2022, **8**(1), 31.

7 W. Gröbner and N. Zöllner, The influence of allopurinol on purine- and pyrimidinesynthesis (author's transl), *Klin. Wochenschr.*, 1978, **53**(16), 255–260.

8 M. E. Ernst and M. A. Fravel, Febuxostat: a selective xanthine-oxidase/xanthine-dehydrogenase inhibitor for the management of hyperuricemia in adults with gout, *Clin. Ther.*, 2009, **31**(11), 2503–2518.

9 H. Jeong, E. Choi, A. Suh, M. Yoo and B. Kim, Risk of cardiovascular disease associated with febuxostat *versus* allopurinol use in patients with gout: a retrospective cohort study in Korea, *Rheumatol. Int.*, 2023, **43**(2), 265–281.

10 L. K. Fu, Y. F. Yu, M. G. Gilbert, Z. Y. Wu and P. H. Raven, Gnetaceae, *Flora China*, 1999, **4**, 102–105.

11 T. A. N. Nguyen and T. C. Nguyen, Anti-inflammatory and analgesic effects of *Gnetum montanum* Markgr. on experimental animals, *Viet Nam J. Tradit. Med. Pharm.*, 2023, **01**(47), 41–51.

12 N. T. V. Thanh, H. D. Cuong, B. H. Tai and P. Van Kiem, Stilbene derivatives from *Gnetum montanum* Markgr. with their xanthine oxidase inhibition activity, *Vietnam J. Chem.*, 2024, **62**(6), 766–771.

13 D. T. Loi, *Medicinal Plants and Drugs from Vietnam*, Medical Publishing House, Hanoi, Vietnam, 2006, 662.

14 Q. Vu, Y. N. Le, T. Á. T. Tran, M. A. Tran and T. N. Hoang, Stilbenoid compounds from *Gnetum montanum* Markgr. in Vietnam, *Vietnam J. Agric. Sci.*, 2024, **22**(6), 771–777.

15 Z. Jian-bo, C. Yu-shu, Z. Shu-nian and X. Jia-min, Studies on the chemical constituents of *Gnetum montanum* Markg, *J. Integr. Plant Biol.*, 1989, **31**(11), 878–882.

16 X. M. Li, M. Lin, Y. H. Wang and X. Liu, Four new stilbenoids from the lianas of *Gnetum montanum* f. megalocarpum, *Planta Med.*, 2004, **70**(2), 160–165.

17 F. Martin, T. Grkovic, M. L. Sykes, T. Shelper, V. M. Avery, D. Camp, R. J. Quinn and R. A. Davis, Alkaloids from the Chinese vine *Gnetum montanum*, *J. Nat. Prod.*, 2011, **74**(11), 2425–2430.

18 Y.-M. Zhai, K. Jiang, S.-J. Qu, H.-F. Luo, J.-J. Tan and C.-H. Tan, Structurally diverse stilbene dimers from *Gnetum montanum* Markgr.: studies on the ^{1}H chemical shift differences between dimeric stilbene epimers correlating to the relative configurations, *RSC Adv.*, 2016, **6**(55), 50083–50090.

19 L. Wang, Y. Zhao, L. Zhou and J. Zhou, Lignans from *Gnetum montanum* Markgr. f. *megalocarpua*, *Chem. Nat. Compd.*, 2009, **45**, 424–426.

20 X. Pan, X. Hou, F. Zhang, P. Tang, W. Wan, Z. Su, Y. Yang, W. Wei, Z. Du, J. Deng and E. Hao, *Gnetum montanum* extract induces apoptosis by inhibiting the activation of AKT in SW480 human colon cancer cells, *Pharm. Biol.*, 2022, **60**(1), 915–930.

21 L. Q. Wang, Y. X. Zhao, J.-M. Hu, A.-Q. Jia and J. Zhou, Stilbene derivatives from *Gnetum montanum* Markgr. f. *megalocarpum* Markgr, *Helv. Chim. Acta*, 2008, **91**, 159–164.

22 T. B. N. Trinh, D. H. Le, T. T. K. Nguyen, V. T. Nguyen, M. H. Nguyen, M. Muller, H. T. Pham, V. P. Le and T. K. N. Nguyen, *In vitro* antiviral activities of ethanol and aqueous extracts of Vietnamese traditional medicinal plants against Porcine Epidemic Diarrhea virus: a coronavirus family member, *VirusDisease*, 2021, **32**(4), 797–803.

23 C.-S. Yao, M. Lin, X. Liu and Y.-H. Wang, Stilbene derivatives from *Gnetum cleistostachyum*, *J. Asian Nat. Prod. Res.*, 2005, **7**, 131–137.

24 Y. Maghsoud, C. Dong and G. A. Cisneros, Investigation of the Inhibition Mechanism of Xanthine Oxidoreductase by Oxipurinol: A Computational Study, *J. Chem. Inf. Model.*, 2023, **63**(13), 4190–4206.